The Astrophysical Journal, 845:1 (12pp), 2017 August 10 https://doi.org/10.3847/1538-4357/aa7742

Dynamics of Massive Atmospheres

Rei Chemke and Yohai Kaspi
Department of Earth and Planetary Sciences, Weizmann Institute of Science, 234 Herzl st., 76100, Rehovot, Israel; rei.chemke@weizmann.ac.il
Received 2017 February 19; revised 2017 June 1; accepted 2017 June 1; published 2017 August 4

Abstract

The many recently discovered terrestrial exoplanets are expected to hold a wide range of atmospheric masses. Here the dynamic-thermodynamic effects of atmospheric mass on atmospheric circulation are studied using an idealized global circulation model by systematically varying the atmospheric surface pressure. On an Earth analog planet, an increase in atmospheric mass weakens the Hadley circulation and decreases its latitudinal extent. These changes are found to be related to the reduction of the convective fluxes and net radiative cooling (due to the higher atmospheric heat capacity), which, respectively, cool the upper troposphere at mid-low latitudes and warm the troposphere at high latitudes. These together decrease the meridional temperature gradient, tropopause height and static stability. The reduction of these parameters, which play a key role in affecting the flow properties of the tropical circulation, weakens and contracts the Hadley circulation. The reduction of the meridional temperature gradient also decreases the extraction of mean potential energy to the eddy fields and the mean kinetic energy, which weakens the extratropical circulation. The decrease of the eddy kinetic energy decreases the Rhines wavelength, which is found to follow the meridional jet scale. The contraction of the jet scale in the extratropics results in multiple jets and meridional circulation cells as the atmospheric mass increases.

Key words: methods: numerical – planets and satellites: atmospheres – planets and satellites: terrestrial planets – turbulence

1. Introduction

The vast ongoing discovery of terrestrial exoplanets and the variety of atmospheric formation sources may lead to a wide range of atmospheric masses on these planets (Adams et al. 2008; Elkins-Tanton & Seager 2008). The atmospheric composition is determined by both internal processes (e.g., tectonic degassing, hydrodynamic and thermal escape of light gases, photosynthesis, silicate weathering, nitrification-dentirification, etc.) and external sources (e.g., nebular gases, asteroids and comet impacts, etc.) (Kasting & Catling 2003; Seager 2013). Even in our solar system, atmospheric mass varies by orders of magnitude among the different planets. For example, while Venus' atmospheric mass is 92 times heavier than Earth's, Mars's atmospheric mass is 166 times lighter.

Atmospheric mass not only varies among different planets, but also planets may be subject to changes in their own surface pressure during their evolution. For example, while several studies argued that high levels of N_2 may have resulted in a heavier atmosphere during Earth's early history (during the late Archean, ∼3 billion years ago) up to 10 times its present-day value (Goldblatt et al. 2009; Johnson & Goldblatt 2015; Kavanagh & Goldblatt 2015), others argued that Earth's atmospheric mass was as light as half its present-day value (Som et al. 2012; Marty et al. 2013; Som et al. 2016). Atmospheric mass is also affected by the mixing ratio of condensible gases (Pierrehumbert & Ding 2016). Controlled by the temperature, the mass flux of condensible gases from an ocean reservoir, and back through precipitation, alter the mass of the atmosphere. Of such examples are the methane cycle on Titan (Lorenz et al. 1999) and the high levels of carbon dioxide in the early Mars atmosphere, super-Earth like GJ581d (which was discovered around the red dwarf Gliese 581, Wordsworth et al. 2011), and in warm periods in the early Earth (Pierrehumbert et al. 2010).

Atmospheric mass shields the surface from extreme short-wave radiation, enables heat transport from warm to cold regions, and through the greenhouse effect enables liquid water to be kept at the planet's surface (Forget & Pierrehumbert 1997; Selsis et al. 2007; Seager 2013). Thus, different atmospheric masses may result in various atmospheric thermodynamic and dynamic properties of the flow (Kaspi & Showman 2015; Chemke et al. 2016b), which affect the planet's habitability (Charnay et al. 2013; Wolf & Toon 2014; Chemke et al. 2016b). For example, it has been suggested that even low insolation terrestrial exoplanets (e.g., Super-Earth like GJ581d) may sustain liquid water on their surface under high atmospheric mass (i.e., high concentrations of greenhouse gases; von Paris et al. 2010; Wordsworth et al. 2010; Kaltenegger et al. 2011; Wordsworth et al. 2011).

Because atmospheric mass plays a crucial role in affecting the planet's habitability and may differ from planet to planet both in and out of our solar system, and even during their history (Nishizawa et al. 2007; Goldblatt et al. 2009; Som et al. 2012; Marty et al. 2013; Johnson & Goldblatt 2015; Kavanagh & Goldblatt 2015; Som et al. 2016), this study aims to better understand the physics behind the different flow regimes under a range of atmospheric masses.

Among the different planetary parameters that may vary from planet to planet, atmospheric mass was found to increase the surface temperature (e.g., Charnay et al. 2013; Wolf & Toon 2014; Kaspi & Showman 2015; Chemke et al. 2016b). This warming has been related to three processes: (1) an increase in atmospheric mass results in pressure broadening of the absorption lines of greenhouse gases, which was found to overcome the increase in molecular (Rayleigh) scattering with atmospheric mass (Goldblatt et al. 2009; Wolf & Toon 2014), (2) higher surface pressure results in a less stable moist adiabatic lapse rate—as the moist adiabatic lapse rate approaches the environmental lapse rate, the convective fluxes weaken, and thus leaving more heat at the surface (Goldblatt et al. 2009;

Charnay et al. 2013)—and (3) higher atmospheric mass increases the heat capacity of the atmosphere, and thus decreases the surface net radiative cooling (warming) effect in the extratropics (tropics; Chemke et al. 2016b). The latter not only increases the global mean surface temperature, but also decreases the surface meridional temperature gradient (Kaspi & Showman 2015; Chemke et al. 2016b). The reduction in the surface meridional temperature gradient is also associated with a reduction of the extratropical vertical eddy fluxes, which further flattens the surface gradient (i.e., less heat is being transported upward).

In a series of simulations, Kaspi & Showman (2015) showed that the atmospheric mass not only modulates the surface temperature, but also affects the strength of the atmospheric circulation. As the atmospheric mass increases, the mean zonal wind decreases together with the eddy momentum flux convergence, while the mean meridional mass transfer increases. Here, to better understand the dynamics in atmospheres with different masses, we use a three-dimensional idealized global circulation model (GCM). Because this model does not take into account processes that are less relevant for the effects of atmospheric mass on its dynamics (e.g., aerosols, chemical reactions, the diurnal and seasonal cycles), its idealization enables us not only to simulate the overall dynamics, but also to isolate the vertical and meridional dynamical and thermodynamical features of the atmosphere with different atmospheric masses.

Section 2 describes the idealized GCM used in this study and the analysis method used to estimate the effects of atmospheric mass on the general circulation. Section 3 discusses the effects of atmospheric mass on the width and strength of the mean tropical circulation. Section 4 studies the effects of atmospheric mass on the strength of the extratropical circulation, by investigating the energy cycle, and on the width of extratropical jets. Section 5 summarizes these results.

2. Methodology

The idealized GCM is a three-dimensional aquaplanet model that solves the primitive equations of an ideal gas atmosphere on a sphere. It is based on the Geophysical Fluid Dynamics Laboratory flexible modeling system and its full description is given in Frierson et al. (2006). At the top of the atmosphere, the solar radiation is latitudinally parametrized using the second Legendre polynomial, and exponentially decays to the surface where it is reflected by a constant planetary albedo of 0.36. The surface is an ocean slab with no dynamics that exchanges heat, moisture and momentum with the lowest atmospheric layer. Using a two-stream gray radiation scheme (Held 1982; Goody & Yung 1995), the longwave radiation is calculated with an optical thickness that is a function of latitude and sigma, $\sigma = pp_s^{-1}$ (pressure normalized by surface pressure). Thus, changing the surface pressure does not affect the spatial structure of the longwave optical thickness, nor does it account for pressure broadening and Rayleigh scattering effects. Each simulation runs with 30 vertical layers and T85 horizontal resolution ($1.^{\circ}4 \times 1.^{\circ}4$).

The atmospheric mass per unit area can be calculated using hydrostatic balance (Hartmann 1994), as $\triangle m = p_s g^{-1}$, where p_s is the surface pressure and g is the gravitational acceleration. For studying the effects of the atmospheric mass on its circulation, a series of simulations are conducted, where the surface pressure is varied between 0.5 and 100 bar (0.5, 1, 3, 5, 7, 10, 15, 20, 30, 50, 100), while the gravitational acceleration is kept constant ($g = 9.81$), similar to Kaspi & Showman (2015). Alternatively, varying the gravitational acceleration (different mean density of the solid plant) and keeping the surface pressure constant would also enable the study of the effects of atmospheric mass. In order to keep the analysis and simulations as simple as possible in the vast planetary parameter space, we keep all planetary parameters similar to those of Earth, and only vary the surface pressure. Because changes in surface pressure affect the time needed to reach kinetic and thermal statistically steady states, the results of each simulation represent the last 1000 days of each run after reaching statistically steady state (e.g., for the most massive atmosphere simulation with $p_s = 100$ bar, the statistically steady state is reached after 20,000 days).

The top row in Figure 1 shows the zonal and time mean meridional streamfunction (color),

$$\Psi = 2\pi a \int_0^1 \bar{v} \cos\varphi d\sigma, \quad (1)$$

where a is Earth's radius, v is the meridional velocity, φ is latitude, and overbar ($\bar{}$) represents a zonal and time mean; and the mean zonal wind, $\bar{u}$ (contours), as a function of sigma and latitude for four simulations with different surface pressure (1, 10, 30, and 100 bar in panels (a), (b), (c), and (d), respectively). The blue (red) colors correspond to clockwise (counterclockwise) circulation. Note that Equation (1) is not the conventional definition of the mean meridional Eulerian mass streamfunction, as here it is normalized by the atmospheric mass ($p_s g^{-1}$).

The 1 bar simulation (Figure 1(a)), which represents Earth's present-day atmosphere, has two major zonally symmetric meridional cells in each hemisphere; the tropical Hadley cell and extratropical Ferrel cell (as in Earth's atmosphere, disregarding the seasonal cycle). The Hadley cell (most equatorward blue colors in Figure 1(a)) is driven by the differential heating between low and high latitudes, which results in rising warm air at the equatorial troposphere. The stable stratosphere above the tropopause halts this equatorial ascending air, which then propagates poleward, cools, and descends at the subtropics. As the poleward movement flow at the upper branch of the Hadley cell roughly conserves mean angular momentum, while its distance from the planet's axis of rotation decreases, a strong zonal flow forms at the edge of the Hadley cell. This flow is referred to as the subtropical jet.

In the extratropics, the circulation is driven by eddies (deviations from the zonal mean), which maintain the indirect circulation of the Ferrel cell by meridionally transferring heat and momentum. The eddies are driven by baroclinic instability (e.g., meridional temperature gradient, Pedlosky 1987), and in their life cycle go through growing and decaying phases (Simmons & Hoskins 1978). In their growing phase, the eddies extract available potential energy from the mean flow and grow at the expense of the meridional temperature gradient (through eddy heat fluxes). Because the meridional temperature gradient is directly related to the vertical shear of the zonal wind, through thermal wind balance, the eddies act to weaken the vertical shear in their growing phase as well. Then, by converting their available potential energy to kinetic energy, the eddies return the energy to the mean flow by strengthening the mean zonal shear through eddy momentum flux convergence, thus maintaining the extratropical eddy-driven jets (Schneider 2006; Vallis 2006).

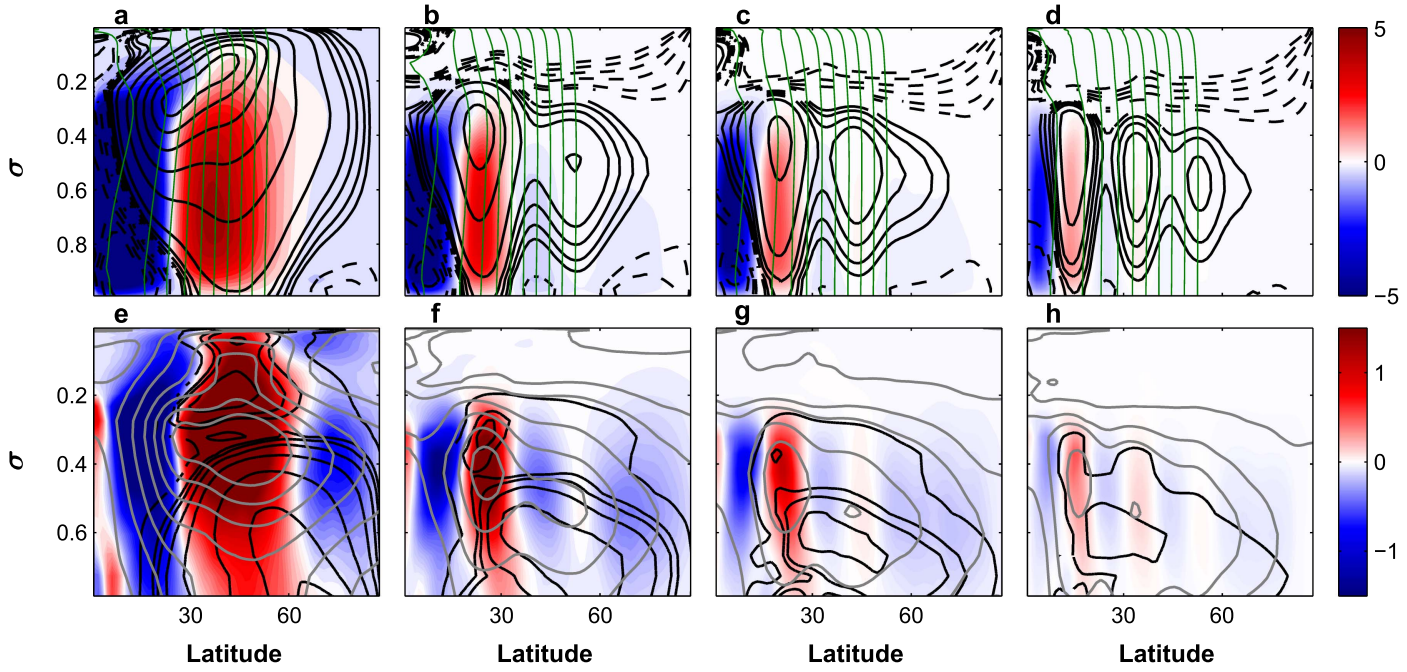

Figure 1. Mean fields from simulations of 1 bar (first column), 10 bar (second column), 30 bar (third column), and 100 bar (fourth column) as a function of sigma and latitude. First row (a)–(d) shows the mean meridional stream function (10^5 m^2 s^{-1}, colors), mean zonal wind (m s^{-1}, black contours), and mean angular momentum (m^2 s^{-1}, green lines). Solid and dashed contours correspond to positive (westerly) and negative (easterly) flows, respectively. The mean angular momentum lines have maximum and minimum values of 2.9×10^9 m^2 s^{-1} and 1.1×10^9 m^2 s^{-1}, respectively, with constant spacing of 0.2×10^9 m^2 s^{-1}. Second row (e)–(h) shows the meridional (10^{-5} m s^{-2}, colors) and vertical (m s^{-2}, black contours) components of the divergence of the EP flux (Equations (11) and (12)) and the mean eddy kinetic energy per unit mass (gray contours).

3. Tropical Circulation

Increasing atmospheric mass results in two robust changes of the mean tropical circulation (Figure 1). First, the circulation contracts as the atmospheric mass increases. Second, the strength of the mean meridional circulation decreases as the atmospheric mass increases. Note that, different from Kaspi & Showman (2015), here we do not plot the mean meridional mass streamfunction, which was shown to increase with atmospheric mass (i.e., mass transfer increases with atmospheric mass), but rather only the strength of the mean circulation.

3.1. Hadley Cell Width

To understand the contraction of the Hadley cell with atmospheric mass (most left blue colors in the top row of Figure 1), we first scale the latitudinal extent of the Hadley cell, and then study the different scalings as a function of atmospheric mass. Figure 2(a) shows the latitudinal extent of the Hadley cell, calculated as the latitude where the mean meridional streamfunction first changes sign at the height of its maximum value, as a function of the surface pressure. The Hadley cell width decreases with atmospheric mass following $\propto p_s^{-0.16}$.

The first scaling studied here for the Hadley cell width is that of Held & Hou (1980), which assumes that the upper branch of the Hadley cell conserves mean angular momentum and that the cell is thermally closed. They suggested that the latitudinal extent of the Hadley cell scales as

$$Y_{\rm HH} \propto \left(\frac{5\Delta_h \theta g H|_{\rm Hadley}}{3\Omega^2 a^2 \theta_0} \right)^{1/2}, \qquad (2)$$

where $\Delta_h\theta$ is the tropospheric equator-to-pole potential temperature difference, Ω is Earth's rotation rate, θ_0 is the global mean tropospheric potential temperature, and $H|_{\rm Hadley}$ is the mean tropopause height in the Hadley cell. In the troposphere, the potential temperature is dynamically distributed from the surface up to the tropopause height, such that the radiative forcing (which balances the dynamics) has a strong vertical dependence (e.g., Schneider & Walker 2006). The tropopause height is thus estimated as the lowest level where above it the radiative relaxation rate, $c_r = \left| \frac{\partial}{\partial p}\left(\overline{Q_{\rm rad}} \left(\frac{\overline{\partial\theta}}{\partial p} \right)^{-1} \right) \right|$, is smaller than $(60\,{\rm days})^{-1}$, where $Q_{\rm rad}$ is the heating due to solar and longwave radiation. Thus, a weaker dynamical or radiative vertical distribution of potential temperature results in a weaker dependence of these fluxes with height, which lowers the tropopause height. Calculating the tropopause height following the definition of the World Meteorological Organization (WMO), as the lowest height where the temperature lapse rate decreases below $2\,{\rm K\,km^{-1}}$, produces similar results through most simulations. However, at high atmospheric mass simulations the WMO definition does not capture well the dynamics in the troposphere.

The Held & Hou (1980) scaling for the latitudinal extent of the Hadley cell (Equation (2)), with a constant of proportionality of $C_{\rm HH} = 1.02$, is found to linearly follow the Hadley cell's edge in our simulations (red dots in Figure 2(b)), $y_{\rm HH} = x + 2.3$ with $R^2 = 0.96$. The 2.3 degree difference between the two scaling might be either related to the Held & Hou (1980) theory assumptions, or to the fact that in Held & Hou (1980) the $\Delta_h\theta$ is calculated as the radiative equilibrium

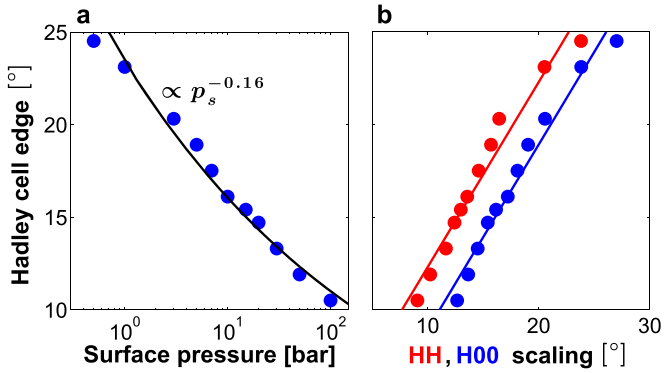

Figure 2. Hadley cell edge (latitude, see the text for a definition), as a function of (a) surface pressure (bar) and (b) Held & Hou (1980) scaling (Equation (2), red) and Held (2000) scaling (Equation (5), blue). The red and blue lines in panel (b) show the best linear fit and correspond to $y_{\rm HH} = x + 2.3$ with $R^2 = 0.96$ and $y_{\rm H00} = x - 1.1$ with $R^2 = 0.97$, respectively.

temperature difference, while here it is the thermodynamic steady-state temperature difference.

The major difference between the Held & Hou (1980) theory and our simulations is the presence of eddies in the later, which may explain the deviation from the Held & Hou (1980) scaling. The time and zonal mean angular momentum equation, after neglecting the vertical advection and frictional processes, can be written as

$$\frac{1}{a\cos\varphi}\frac{\partial}{\partial\varphi}(\overline{v}\overline{m}\cos\varphi) = -\frac{1}{a\cos\varphi}\frac{\partial}{\partial\varphi}(\overline{v'm'}\cos\varphi), \quad (3)$$

where $m = (u + \Omega a\cos\varphi)a\cos\varphi$ is angular momentum and prime denotes deviation from zonal mean (i.e., the eddy component). The eddies (right-hand side of Equation (3)), thus, may overcome the conservation of mean angular momentum on a poleward moving air parcel, which may result in deviations from Held & Hou (1980). To examine this, the mean angular momentum is plotted in Figures 1(a)–(d) (green lines). The mean angular momentum is not entirely conserved at the upper branch of the Hadley cell (i.e., streamfunction lines cross mean angular momentum lines), which may explain the 2.3° difference between the two scalings. Nonetheless, the mean angular momentum is more conserved in the Hadley cell than in the extratropics, as its meridional derivative is much smaller at the Hadley cell (note that the spacing between the mean angular momentum lines is constant). To assess the role of eddies on the mean circulation in comparison to the role of diabatic heating, we next study their effects on the mean streamfunction in a series of atmospheric mass simulations.

Using quasi-geostrophic theory on a β-plane, Holton (1992) derived a diagnostic elliptic equation for the streamfunction, $\overline{\chi}$,

$$\frac{N_h^2}{\rho_0}\frac{\partial^2\overline{\chi}}{\partial y^2} + f_0^2\frac{\partial}{\partial z}\left(\frac{1}{\rho_0}\frac{\partial\overline{\chi}}{\partial z}\right) = \frac{\kappa}{H_0}\frac{\partial J}{\partial y} - \frac{R_d}{H_0}\frac{\partial\overline{v'T'}}{\partial y}, \quad (4a)$$

$$-f_0\frac{\partial^2\overline{u'v'}}{\partial z\partial y} + \frac{\partial\overline{X}}{\partial z}, \quad (4b)$$

where $-\rho_0 v = \frac{\partial\overline{\chi}}{\partial z}$ and $\rho_0 w = \frac{\partial\overline{\chi}}{\partial y}$, ρ_0 is a reference profile of the density, $N_h^2 = \frac{R_d}{H_0}\left(\frac{\kappa T_0}{H_0} + \frac{\partial T_0}{\partial z}\right)$, where $\kappa = R_d/C_p$, with $R_d = 287\ \mathrm{J\,kg^{-1}\,K^{-1}}$ and $C_p = 1004\ \mathrm{J\,kg^{-1}\,K^{-1}}$ are the gas constant of dry air and the specific heat of air, respectively, $H_0 = \frac{R_d T_s}{g}$ is the scale height, where T_s is the global averaged temperature, and T_0 is a reference profile of the temperature. $J = \frac{N_h^2 H_0}{R_d}\overline{w} + \frac{\partial\overline{v'T'}}{\partial y}$ is the diabatic heating, where $\overline{w}$ is the mean vertical velocity in z coordinates and $\overline{X}$ represents momentum loss due to dissipation. The elliptic equation is proportional to $-\overline{\chi}$, as the latter can be represented using double Fourier series in y and z. For assessing the role of eddies on the mean circulation, the first three terms on the right-hand side of Equation (4) are plotted for three atmospheric mass simulations (Figure 3). Through all simulations, the dominant term that contributes mostly to the Hadley circulation is the diabatic term (first row in Figure 3), as suggested in the Held & Hou (1980) theory, while the eddy terms play an important role mostly in the extratropics (maintaining the Ferrel circulation, second and third rows in Figure 3). As the atmospheric mass increases, the eddy fields weaken (Section 4), resulting in a clearer conservation of the mean angular momentum (green lines in Figures 1(a)–(d)).

In summary, even though eddies play a role in the mean angular momentum budget, the latter shows minor variations with latitude in the Hadley cell. This together with the fact the Hadley circulation is mostly driven by diabatic heating may explain why the scaling of Held & Hou (1980) works relatively well in these simulations (red dots in Figure 2(b)).

The effects of eddies on the Hadley circulation led Held (2000) to introduce a second scaling, which estimated the latitudinal extent of the Hadley cell as the latitude where the vertical shear of the angular momentum conserving flow first encounters the baroclinically unstable shear of the midlatitudes (according to the two-layer model criterion of Phillips 1954),

$$Y_{\rm H00} \propto \left(\frac{NH|_{\rm ET}}{\Omega a}\right)^{1/2}, \quad (5)$$

where $N^2 = -\frac{g^2\rho}{\theta}\frac{\partial\theta}{\partial p}$ and $H|_{\rm ET}$ are the mean extratropical static stability and tropopause height, respectively. The scaling of Held (2000; Equation (5)) with a proportionality constant of $C_{\rm H00} = 0.78$ is also found to linearly follow the Hadley cell edge in our simulations (blue dots in Figure 2(b)), $y_{\rm H00} = x - 1.1$ with $R^2 = 0.97$, but with a poleward bias rather than an equatorward bias when using Equation (2).

The linear relation of both scalings (Figure 2(b)) with the latitudinal extent of the Hadley cell enables further investigation of its decrease with atmospheric mass, by studying the different components of each scaling. To understand which of the components of each scaling contributes most to the contraction of the Hadley cell, we normalize both Equations (2) and (5) by their values in the most massive simulation of 100 bar surface pressure, and take the logarithm of the equations. This produces the following two equations,

$$\log\left(\frac{Y_{\rm HH}}{Y_{\rm HH_{100}}}\right) = 0.5\log\left(\frac{\Delta_h\theta}{\Delta_h\theta_{100}}\right) + 0.5\log\left(\frac{H|_{\rm Hadley}}{H|_{\rm Hadley_{100}}}\right) + 0.5\log\left(\frac{\theta_{0_{100}}}{\theta_0}\right), \quad (6)$$

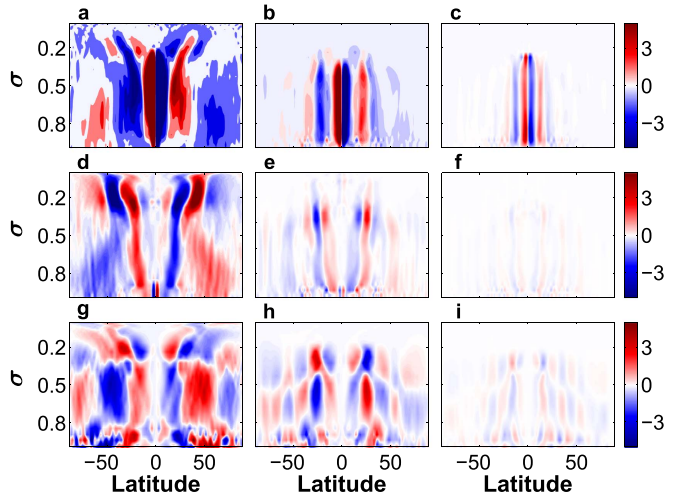

Figure 3. Forcing terms of the stream function equation (10^{-13} s^{-3}, Equation (4)) from simulations of 1 bar (first column), 10 bar (second column), and 100 bar (third column) as a function of sigma and latitude. First row (a)–(c) shows the diabatic heating, second row (d)–(f) shows eddy temperature fluxes, and third row (g)–(i) shows eddy momentum fluxes.

and

$$\log\left(\frac{Y_{\mathrm{H00}}}{Y_{\mathrm{H00}_{100}}}\right) = 0.5\log\left(\frac{N}{N_{100}}\right) + 0.5\log\left(\frac{H|_{\mathrm{ET}}}{H|_{ET_{100}}}\right), \qquad (7)$$

where all the contributions from variables that do not change with atmospheric mass (e.g., rotation rate, radius, gravitational acceleration) vanish. Plotting the above components as a function of surface pressure (Figure 4) shows that 80% of the decrease in the Held & Hou (1980) scaling (black dots in Figure 4(a)) can be explained by the decrease of the tropospheric equator-to-pole potential temperature difference ($\Delta_h\theta$, blue dots in Figure 4(a)) and the other 20% by the decrease in the mean tropopause height in the Hadley cell ($H|_{\mathrm{Hadley}}$, red dots in Figure 4(a)). For the Held (2000) scaling (black dots in Figure 4(b)) two-thirds of the decrease in his scaling can be explained using the reduction of the mean extratropical static stability (N, blue dots in Figure 4(b)), and one-third using the reduction of the tropopause height at the edge of the Hadley cell ($H|_{\mathrm{ET}}$, red dots in Figure 4(b)).

This indicates that the reductions in the meridional temperature gradient, tropopause height, and static stability in the tropics and in the extratropics (Figure 4), are strongly related to the decrease in the scaling of the Hadley cell width (Figure 2). Figure 5(a) shows the temperature difference between two simulations of different atmospheric mass ($T_{20\ \mathrm{bar}} - T_{1\ \mathrm{bar}}$). The contours correspond to the mean streamfunction from the simulation with a surface pressure of 20 bar, where the solid and dashed contours, respectively, correspond to counterclockwise and clockwise circulation. The purple and green lines show the tropopause height in the simulation of 1 bar and 20 bar surface pressure, respectively.

As the atmospheric mass increases, the temperature increases substantially in the extratropics, less strongly near the surface at low latitudes, and decreases at low latitudes below the tropopause. This results in two main outcomes. First, the mean tropospheric meridional temperature gradient decreases, as shown in Figure 4(a) (blue dots), and second, at low-mid

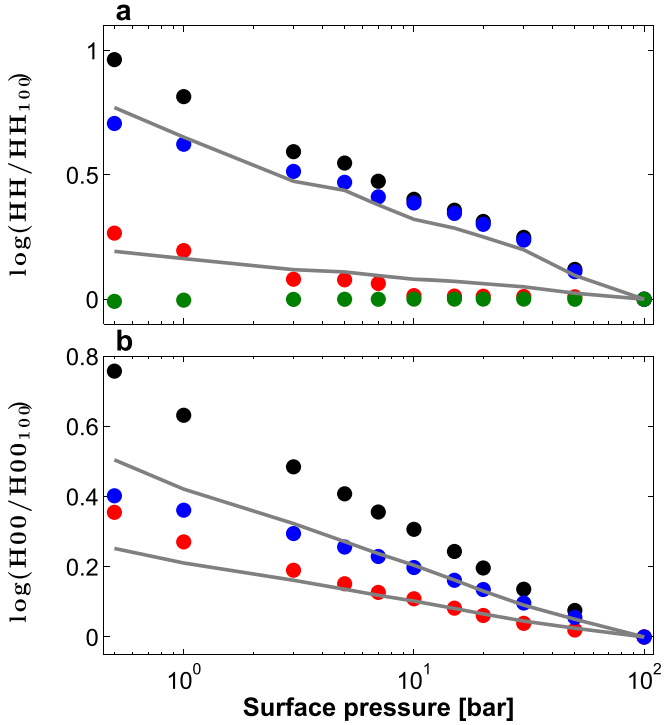

Figure 4. Log of the ratio of (a) the HH scaling (Held & Hou 1980; black), tropospheric equator-to-pole potential temperature difference ($\Delta_h\theta$, blue), tropopause height in the Hadley cell ($H|_{\mathrm{Hadley}}$, red) and the global mean tropospheric potential temperature (θ_0, green), and (b) the H00 scaling (Held 2000; black), the extratropical static stability (N, blue) and tropopause height ($H|_{\mathrm{ET}}$, red) with their corresponding values in the most massive atmosphere simulation (100 bar surface pressure) as a function of surface pressure (bar). In panels (a) and (b), the gray lines show the 0.8 and 0.2 and the 0.6 and 0.3 values of the black dots, respectively.

latitudes the vertical temperature gradient increases. The increase of the temperature lapse rate can also be seen in Figures 5(b) and (c), where the vertical temperature profiles at the edge of the Hadley cell (red lines) and at midlatitudes (∼40°, blue lines) are shown for simulations of 1 bar (solid lines) and 20 bar (dashed lines) surface pressure. At low-mid latitudes, due to the warming of lower layers and cooling of the upper layers, the temperature lapse rate increases as the atmospheric mass increases (compare solid and dashed red lines in Figure 5(b)). Similarly, at high latitudes, the lower troposphere warms more than the upper troposphere, which also increases the temperature lapse rate with atmospheric mass (compare solid and dashed blue lines in Figure 5(c)). The increase in the lapse rate with atmospheric mass reduces the static stability (N), resulting in a less stable atmosphere (blue dots in Figure 4(b)). This decrease in the potential temperature lapse rate through all latitudes indicates a weaker vertical distribution of potential temperature, which results in a lower tropopause height (compare the purple and green lines in Figure 5(a)) as was shown in Figure 4 (red dots) and is further discussed below.

What are the mechanisms behind the tropospheric cooling of low-mid latitudes, and the warming of low altitudes and high latitudes? Understanding these temperature changes with atmospheric mass can further elucidate the changes in tropopause height and meridional and vertical temperature gradients, and the contraction of the Hadley cell. The effects of surface pressure on the temperature can be understood by

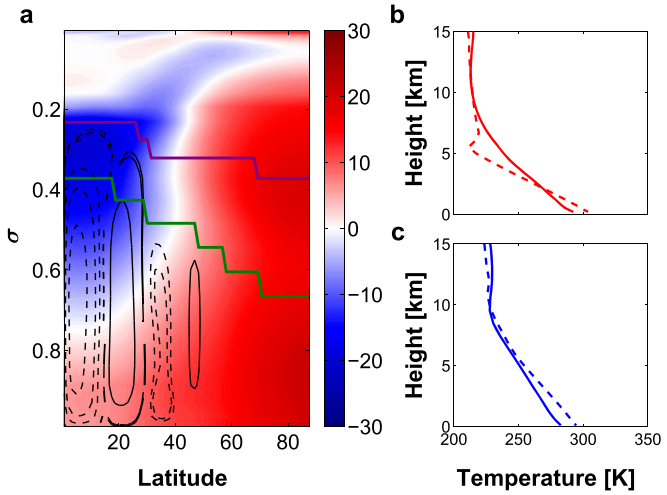

Figure 5. (a) Mean temperature difference (K, colors) between simulations with surface pressure of 20 bar and 1 bar as a function of sigma (p/p_s) and latitude. The solid and dashed lines, respectively, show the counterclockwise and clockwise circulation based on the stream function ($m^2\ s^{-1}$) in the simulation with surface pressure of 20 bar. The purple and green lines show the tropopause height in the simulation with surface pressure of 1 bar and 20 bar, respectively. Panels (b) and (c) show, respectively, the tropical (at the edge of the Hadley cell, red lines) and extratropical (~40°, blue lines) temperature profiles (K) as a function of height (km). The solid and dashed lines correspond to simulations with surface pressure of 1 bar and 20 bar, respectively.

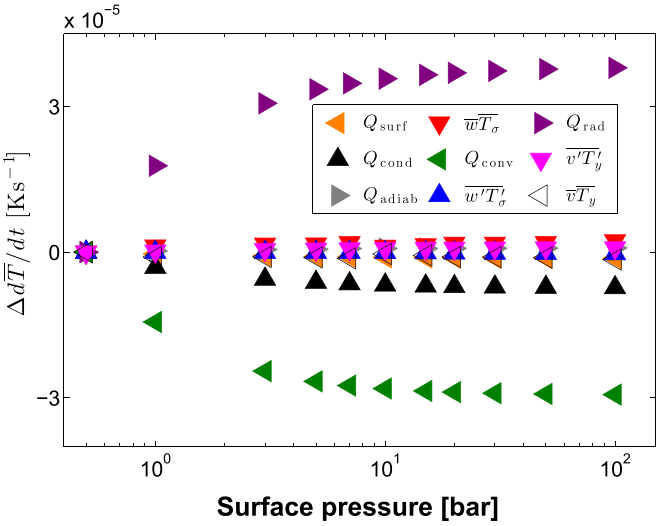

Figure 6. Mean tropospheric components of the temperature tendency equation (Ks^{-1}) relative to the lightest atmosphere simulation (0.5 bar surface pressure) as a function of surface pressure (bar), radiation (purple), vertical advection of eddy temperature fluxes (blue), adiabatic term (gray), vertical advection of mean temperature fluxes (red), meridional advection of mean temperature fluxes (black), meridional advection of eddy temperature fluxes (magenta), surface fluxes (orange), condensation (black), and convection (green).

studying the temperature tendency equation,

$$\frac{\partial T}{\partial t} = -\boldsymbol{u}\cdot\nabla T + Q_{\rm adiab} + Q_{\rm conv} + Q_{\rm cond} + Q_{\rm rad} + Q_{\rm surf}, \tag{8}$$

where T is the temperature field, $\boldsymbol{u}$ is the three-dimensional velocity vector, and the adiabatic heating is $Q_{\rm adiab} = \frac{\kappa T\omega}{p}$, where ω is the vertical velocity in pressure coordinates. Latent heat release per unit mass is calculated through convection ($Q_{\rm conv}$) and condensation ($Q_{\rm cond}$) processes, respectively (Betts 1986; Betts & Miller 1986). The convection scheme relaxes the water vapor toward a profile of 70% relative humidity of the moist adiabatic lapse rate. The condensation scheme prevents the specific humidity from exceeding saturation by precipitating the condensed water vapor (Frierson et al. 2006). Vapor saturation is calculated using the Clausius–Clapeyron relation. The heating due to solar and longwave radiation ($Q_{\rm rad}$) is calculated as

$$Q_{\rm rad} = \frac{1}{\rm C_p}\frac{d(Q_{\rm s}-Q_{\rm l})}{d{\rm m}}, \tag{9}$$

where $Q_{\rm s}$ and $Q_{\rm l}$ are the net solar and longwave fluxes, respectively, and $dm = dpg^{-1}$ is the mass of the atmosphere between two adjacent layers. Heat exchange between the slab ocean and the lowest atmospheric level, through diffusive and heat fluxes, are calculated in $Q_{\rm surf}$.

Note, that studying the effects of atmospheric mass on the temperature field using the energy equation and not the temperature equation is problematic, since the translation between energy and temperature is changing between simulations with different atmospheric mass (due to the atmospheric heat capacity). Thus, an increase in the energy fluxes does not necessarily imply an increase in the temperature (as the energy fluxes are needed to be normalized by the atmospheric heat capacity, $C_p dm$, in order to indicate the changes in the temperature field).

Figure 6 shows the tropospheric mean of the terms on the right-hand side of Equation (8) as a function of surface pressure, with respect to the lightest atmospheric mass simulation with a surface pressure of 0.5 bar. At steady state, the left-hand side of Equation (8) is zero, thus the sum of all components at each surface pressure simulation is zero. The term that contributes mostly to warming the troposphere is the radiative term (purple triangles, Equation (9)), which is mainly balanced by cooling due to convective processes (green triangles).

An increase in atmospheric mass increases the heat capacity of the atmosphere, and following Equation (9), tends to decrease the net radiative forcing (Chemke et al. 2016b). This decrease weakens the radiative forcing vertical dependence, which decreases the tropopause height (blue dots in Figures 4(a) and (b)). In addition, at places where there is a net radiative cooling, the radiation term acts to cool the atmosphere at a lesser rate. Because net radiative cooling occurs through most of the troposphere, except near the surface around the equator, most of the troposphere warms as the atmospheric mass increases (red colors in Figure 5(a)). Moreover, since in the lower atmosphere net radiative cooling is more pronounced in the extratropics, heating becomes stronger at higher latitudes, and contributes both to the reduction in the meridional temperature gradient (blue dots in Figure 4(a)), and to the increase of the lapse rate at high latitudes (Figure 5(c)), and thus to the decrease of the static stability (blue dots in Figure 4(b)).

The convective scheme in the model acts to relax the temperature profile toward a moist adiabatic lapse rate from the lifting condensation level up to the level of zero buoyancy (Betts 1986; Betts & Miller 1986). An increase in surface pressure increases the moist adiabatic lapse rate (due to the dependence of the mixing ratio on pressure), bringing it closer

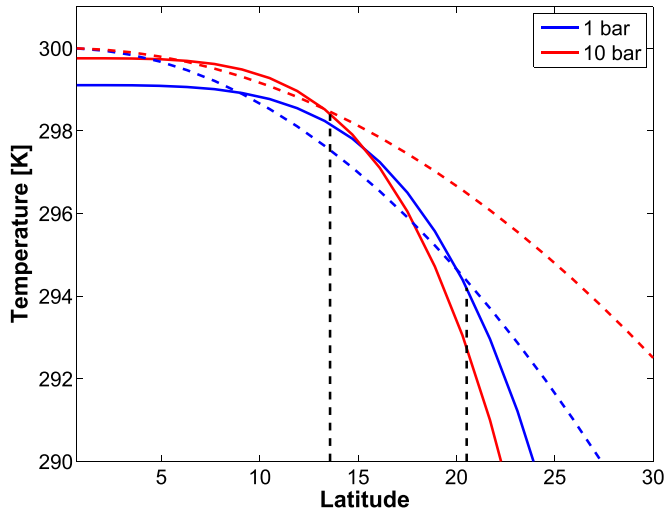

Figure 7. Temperature from the angular momentum conserving solution (θ_m, K, solid lines) and the radiative equilibrium temperature (θ_e, K, dashed lines, with $\theta_{e_0} = 300$ K), from Held & Hou (1980) theory, as a function of latitude for simulations with surface pressure of 1 bar (blue lines) and 10 bar (red lines). The vertical black dashed lines indicate the latitudinal extent of the Hadley cell of 20°.5 and 13°.5 in simulations with surface pressure of 1 bar and 10 bar, respectively.

to the environmental lapse rate (Goldblatt et al. 2009). As the atmospheric mass increases, the convective fluxes thus tend to cool the surface and warm the upper level at a lesser rate (i.e., less heat is transferred upward; blue colors in Figure 5(a), and green triangles in Figure 6). Because convection occurs mostly at low-mid latitudes, this cooling effect of the upper level contributes both to the weakening of the meridional temperature gradient (blue dots in Figure 4(a)) and to an increase in the vertical temperature gradient at low-mid latitudes (Figure 5(b)), which decreases the static stability (blue dots in Figure 4(b)). This reduction in convective fluxes weakens its vertical dependence, which thus decreases the tropopause height at low-mid latitudes (blue dots in Figure 4(a)). Note that at low latitudes the convective fluxes and radiative cooling have opposite effects to, respectively, increase and decrease the vertical temperature gradient with atmospheric mass. These opposite tendencies may also imply the response of the convective fluxes to changes in the radiative fluxes. Because the terms in Equation (8) must be in balance at steady state, a reduction in radiative cooling, may result in a reduction in convective warming, regardless of their dependence on atmospheric mass. Determining cause and effect are beyond the scope of this study.

In aggregate, the effect of atmospheric mass to reduce both the convective fluxes and the radiative cooling effect (Figure 6), tends to weaken the meridional temperature gradient, and decrease the tropopause height and the static stability in both low and high latitudes (Figure 5(a)). Following the scaling of both Held & Hou (1980) and Held (2000), and consistent with our simulations, these changes act to contract the latitudinal extent of the Hadley cell (Figures 2 and 4). These effects can also be seen by comparing the temperature solutions from Held & Hou (1980; Figure 7). In their theory, the Hadley cell is thermally closed such that the total radiative equilibrium temperature (i.e., diabatic forcing) in the Hadley cell (dashed lines in Figure 7), $\theta_e = \theta_{e_0} - \Delta_h \theta \varphi^2$, where θ_{e_0} is the equilibrium temperature at the equator, equals the total temperature from the angular momentum conserving solution

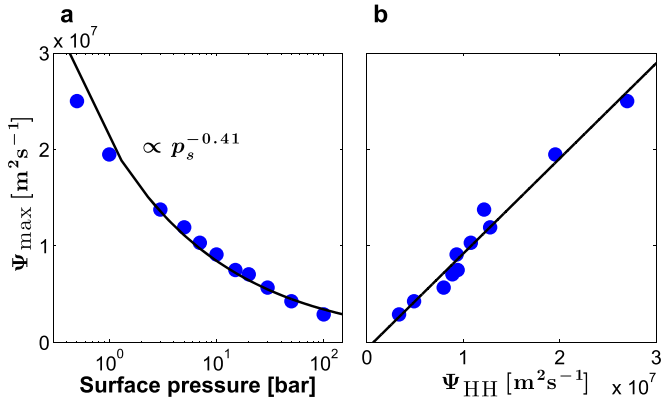

Figure 8. Hadley cell strength, calculated as the maximum absolute value of the stream function (m^2 s^{-1}, Equation (1)), as a function of (a) surface pressure (bar) and (b) Held & Hou (1980) scaling (Equation (10)). The black line in panel (b) shows the best linear fit ($y_{HH_\Psi} = x - 6.48 \times 10^5$, with $R^2 = 0.97$).

(solid lines in Figure 7), $\theta_m = \theta(0) - \frac{\theta_0 \Omega^2 a^2 \varphi^4}{2gH|_{\text{Hadley}}}$, where $\theta(0) = \theta_{e_0} - \frac{5\Delta_h \theta^2 gH|_{\text{Hadley}}}{18\Omega^2 a^2 \theta_0}$ is the potential temperature at the equator. Thus, the Hadley cell edge is predicted by where the solid and dashed lines intersect, such that the areas between the solid and dashed lines are equal inside the Hadley cell. For a given θ_{e_0}, θ_e changes slower with latitude as the atmospheric mass increases (compare blue and red dashed lines in Figure 7), due to the decrease in the meridional temperature gradient with atmospheric mass (Figures 4 and 5), which is associated with the reduction of the radiative cooling effect. θ_m, on the other hand, changes faster with latitude as the atmospheric mass increases (compare blue and red solid lines in Figure 7), due to the decrease in the tropopause height with atmospheric mass (Figures 4 and 5). As the atmospheric mass increases, the steepening of θ_m with latitude together with the more moderate change of θ_e, results in an equatorward shift of the Hadley cell edge (compare vertical black dashed lines in Figure 7).

3.2. Hadley Cell Strength

As was shown in Figures 1(a)–(d), the Hadley circulation weakens with atmospheric mass following $\propto p_s^{-0.41}$ (Figure 8(a)). The Hadley cell strength is calculated as the maximum absolute value of the mean meridional streamfunction (Equation (1)). According to Held & Hou (1980) scaling theory, the strength of the Hadley circulation follows,

$$\Psi \propto \frac{\Delta_h \theta^{2.5} g^{1.5} H^{2.5}|_{\text{Hadley}}}{\Omega^3 a^2 \theta_0^{1.5} \Delta_v \theta}, \tag{10}$$

where $\Delta_v \theta$ is the vertical tropopause-to-surface potential temperature difference averaged over the entire atmosphere. The Hadley cell strength shows a linear relation with the scaling of Held & Hou (1980; Equation (10)) and using a constant of proportionality of $C_{HH_\Psi} = 1.4 \times 10^{-3}$ s^{-1}.

To elucidate which of the components in Equation (10) contributes mostly to the agreement between the Hadley cell strength and the scaling of Held & Hou (1980; Equation (10)), the Hadley cell strength is plotted as a function of each of the Held & Hou (1980) scaling components (Figure 9). While the meridional temperature gradient shows similar scaling to Equation (10) through all atmospheric mass simulations (Figure 9(b)), the tropopause height follows the Held & Hou (1980) scaling mostly

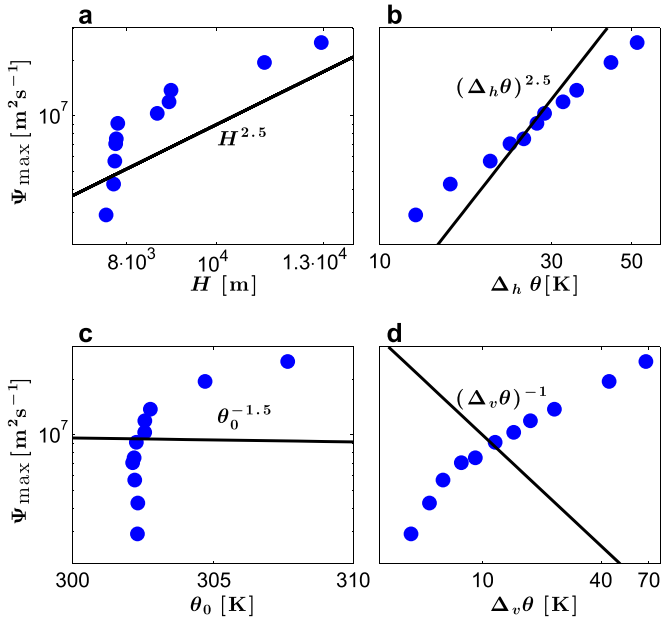

Figure 9. Hadley cell circulation strength (maximum absolute value of the mean meridional stream function, m^2 s^{-1}, Equation (1)) as a function of (a) averaged tropopause height in the Hadley cell ($H|_{\text{Hadley}}$, m), (b) tropospheric equator-to-pole potential temperature difference ($\Delta_h\theta$, K), (c) mean tropospheric potential temperature (θ_0, K), and (d) horizontal mean vertical tropopause-to-surface potential temperature difference ($\Delta_v\theta$, K). The black lines at each panel show the scaling relation based on Held & Hou (1980; Equation (10)).

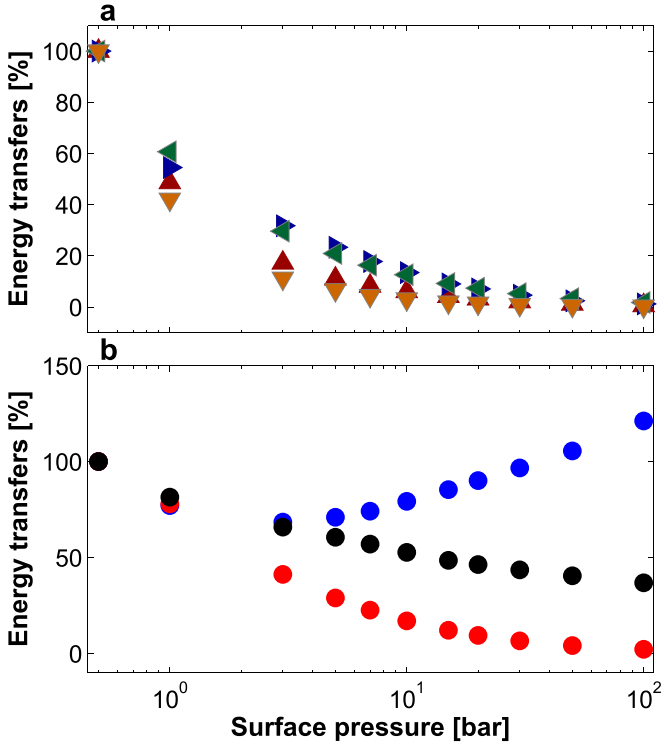

Figure 10. Energy conversions in the Lorenz's energy cycle in percentage of their corresponding values in the lightest atmospheric mass simulation of 0.5 bar as a function of surface pressure (bar); (a) MAPE to EAPE (red, Equation (13)), EAPE to EKE (green, Equation (14)), EKE to MKE (blue, Equation (15)), and MAPE to MKE (orange, Equation (16)). (b) Components of MAPE to EAPE (Equation (13)); Γ (blue), mean meridional temperature gradient (black) and mean meridional eddy temperature flux (red).

in low atmospheric mass simulations (Figure 9(a)). On the other hand, the mean potential temperature (Figure 9(c)) and the vertical temperature gradient (Figure 9(d)) are poorly correlated (and even have an opposite sign) with the scaling of Held & Hou (1980; Equation (10)). Thus, the decrease of both the tropopause height and meridional temperature gradient are the components that contribute mostly to the weakening of the Hadley circulation with atmospheric mass.

4. Extratropical Circulation

4.1. Strength of the Extratropical Circulation

Similar to the mean tropical circulation discussed in Section 3, the mean extratropical circulation and eddy fields also weaken with atmospheric mass (Figure 1). Due to angular momentum conservation, the contraction of the Hadley cell with surface pressure weakens the subtropical jet (i.e., the most equatorward jet, contours in Figures 1(a)–(d)). Concomitantly, not only the subtropical jet weakens but also the eddy-driven jets. Because these jets are maintained by convergence of eddy momentum fluxes, these fluxes also weaken with atmospheric mass (colors in Figures 1(e)–(h)). The bottom row in Figure 1 shows the divergence of the two components of the Eliassen–Palm flux (EP flux, Edmon et al. 1980),

$$-\frac{1}{a\cos^2\varphi}\frac{\partial}{\partial\varphi}(\overline{u'v'}\cos^2\varphi), \tag{11}$$

in colors, and

$$\frac{\partial}{\partial p}\left(f\overline{v'\theta'}\left(\frac{\partial\overline{\theta}}{\partial p}\right)^{-1}\right), \tag{12}$$

in black contours, where f is the Coriolis parameter. The red (blue) colors in Figures 1(e)–(h) correspond to convergence (divergence) of eddy momentum fluxes (Equation (11)), and are associated with the acceleration (deceleration) of the eddy-driven jets (solid contours in Figures 1(a)–(d)). The reduction of the eddy-mean flow interactions is also observed in the vertical component of the EP flux (Equation (12)) as well as in the mean eddy kinetic energy per unit mass, EKE $= \overline{u'^2 + v'^2}$ (gray contours).

Since eddy-mean flow interactions play an important role in the extratropics, studying the eddy-mean energy cycle helps explain the reduction in the strength of both the eddy fields and mean circulation. For each simulation, we calculate the global mean energy conversions of the Lorenz's (1955) energy cycle, following Peixoto & Oort (1992), where

$$\text{MAPE} \rightarrow \text{EAPE} = -C_p\left\langle\frac{\Gamma\overline{v'T'}}{a}\frac{\partial\overline{T}}{\partial\varphi}+p^{-k}\overline{w'T'}\frac{\partial}{\partial p}\Gamma p^k(\overline{T}-[T])\right\rangle \tag{13}$$

is the conversion of mean available potential energy, MAPE $= \langle(\overline{T}^2-[T]^2)\Gamma C_p\rangle$, to eddy available potential energy, EAPE $= \langle\overline{T'^2}\Gamma C_p\rangle$,

$$\text{EAPE} \rightarrow \text{EKE} = -\left\langle\frac{\overline{v'}}{a}\frac{\partial\overline{\phi'}}{\partial\varphi}+\frac{\overline{u'}}{a\cos\varphi}\frac{\partial\overline{\phi'}}{\partial\lambda}\right\rangle \tag{14}$$

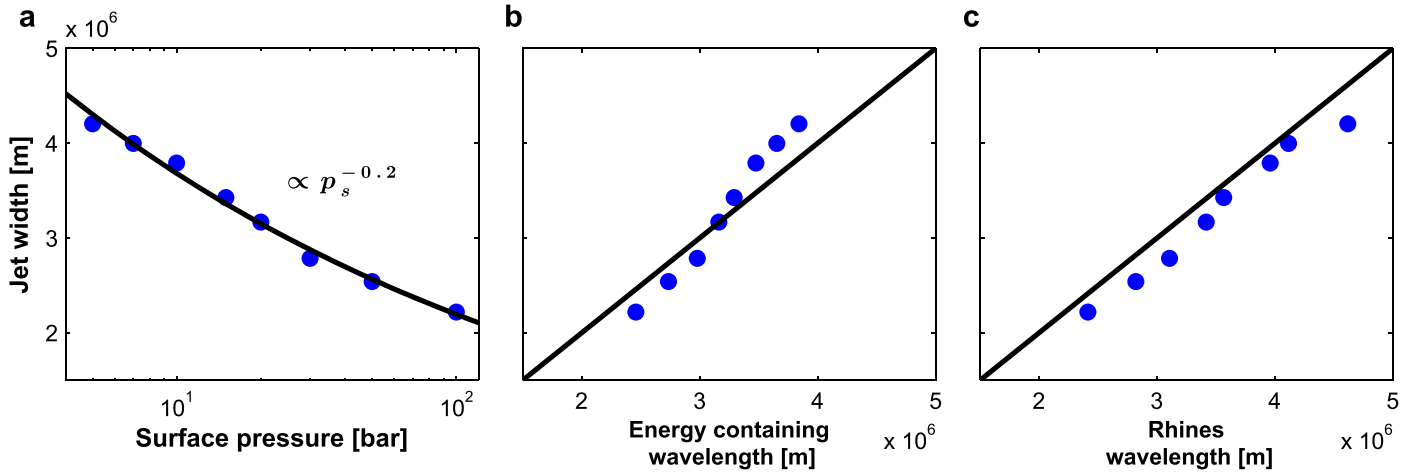

Figure 11. (a) The jet width (m) as a function of (a) surface pressure, (b) the energy-containing wavelength (Equation (18)), and (c) the Rhines wavelength. The jet's width is calculated as the meridional distance between two consecutive minima of the eddy-driven jets. The jets' width is calculated only in simulations where the eddy-driven jets are clearly separated from the subtropical jet ($p_s \geqslant 5$ bar).

is the conversion of EAPE to EKE,

$$\text{EKE} \rightarrow \text{MKE} = \left\langle \frac{\overline{u'v'}\cos\varphi}{a}\frac{\partial(\overline{u}/\cos\varphi)}{\partial\varphi} + \overline{u'w'}\frac{\partial\overline{u}}{\partial p} + \frac{\overline{v'^2}}{a}\frac{\partial\overline{v}}{\partial\varphi} + \overline{v'w'}\frac{\partial\overline{v}}{\partial p} - \frac{\overline{v}\overline{u'^2}\tan\varphi}{a}\right\rangle \tag{15}$$

is the conversion of EKE to mean kinetic energy (MKE $= \overline{u}^2 + \overline{v}^2$), and

$$\text{MAPE} \rightarrow \text{MKE} = -\left\langle \overline{v}\frac{\partial\overline{\phi}}{a\partial\varphi}\right\rangle \tag{16}$$

is the conversion of MAPE to MKE, where squared brackets denote a horizontal mean on a constant vertical level, angle brackets denote a global mean (horizontal and vertical mean) over the entire atmosphere, $\Gamma = -\frac{k\theta}{pT}\left(\frac{\partial[\theta]}{\partial p}\right)^{-1}$, w is the vertical velocity, ϕ is the geopotential, and λ is longitude.

As the atmospheric mass increases, the entire eddy-mean flow energy cycle weakens (Figure 10(a)). The conversions of energy out of the MAPE (red and orange triangles in Figure 10(a)) reduce faster than the conversion of energy in and out of the EKE (blue and green triangles in Figure 10(a)). Since the extratropical circulation is driven by baroclinic instability (e.g., Charney 1947; Eady 1949; Phillips 1954; Charney & Stern 1962; Simmons & Hoskins 1978), a key in understanding the weakening of the entire energy cycle resides in the conversion of MAPE to EAPE (Equation (13)). The dominant term in Equation (13) that contributes mostly to the production of EAPE is $\frac{\Gamma\overline{v'T'}}{a}\frac{\partial\overline{T}}{\partial\varphi}$. Separating the different components of this term shows that, while Γ increases with atmospheric mass (blue dots in Figure 10(b)), the mean meridional eddy temperature flux (red dots in Figure 10(b)), as well as the meridional temperature gradient (black dots in Figure 10(b)), decrease with atmospheric mass. Among these, the mean meridional eddy temperature flux seems to show a stronger and more similar reduction (reducing almost 100% of its value between the most light and heavy atmosphere simulations) as the conversion of MAPE to EAPE (Equation (13)), than the meridional temperature gradient.

The reduction in the meridional temperature gradient is a direct consequence of increasing atmospheric mass, as discussed in Section 3.1, due to the reduction in both the net radiative cooling at high latitudes and convective warming at low latitudes. Assuming that the meridional eddy temperature fluxes are diffusive (e.g., Green 1970; Held 1978; Held & Larichev 1996), a decrease in the meridional temperature gradient results in a weakening of the meridional eddy temperature fluxes, which further weakens the temperature gradient and the energy cycle.

Using hydrostatic balance and assuming small variation of density with latitude, the conversion between MAPE and MKE can be written as $\text{MAPE} \rightarrow \text{MKE} \approx -R_d\left\langle \overline{v}\frac{\partial\overline{T}}{a\partial\varphi}\right\rangle$. This is similar to thermal wind balance, where a decrease in the meridional temperature gradient, is associated with a weakening of the vertical shear of the mean zonal wind. As the winds vanish at the surface, a reduction in the meridional temperature gradient is associated with a decrease in the MKE (i.e., the mean zonal winds, contours in Figures 1(a)–(d)). In summary, the reduction of the mean meridional temperature gradient with atmospheric mass reduces the extraction of MAPE both to the eddy fields and mean flow. The strong baroclinicity of the upper troposphere was found to explain why a reduction in the meridional temperature gradient at these levels (as occurs in our simulations, Figure 5(a)), results in a reduction in the eddy fields as well (Yuval & Kaspi 2016, 2017).

4.2. The Width of the Extratropical Circulation

The extratropical circulation not only shifts equatorward together with the contraction of the Hadley cell as the atmospheric mass increases, but also contracts, leading to the formation of multiple alternating extratropical circulations (Figure 1). Concomitantly, the jets' width decreases with atmospheric mass following $\propto p_s^{-0.2}$ (Figure 11(a)). The jets' width is calculated as the meridional distance between two consecutive minima of the eddy-driven jets. This leads to multiple consecutive direct and indirect cells (colors in Figures 1(a)–(d)), eddy-driven jets (contours in Figures 1(a)–(d)) along with their corresponding

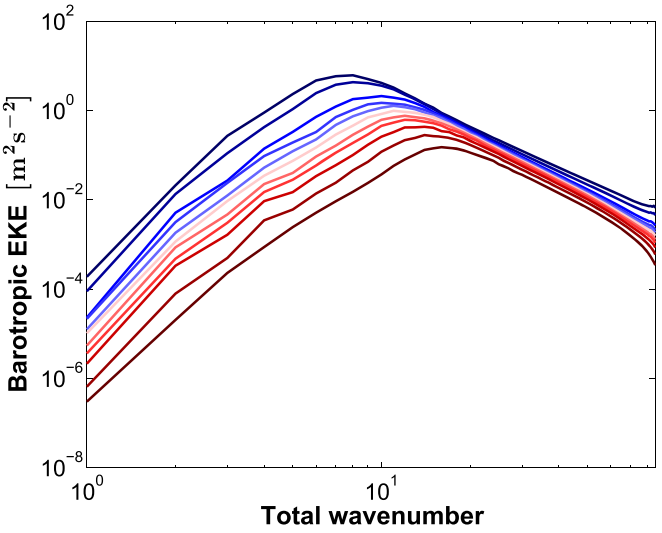

Figure 12. (a) The spectrum of the barotropic eddy kinetic energy (bEKE, $m^2 s^{-2}$) as a function of total wavenumber for different atmospheric mass simulations. Red (blue) colors correspond to heavier (lighter) atmospheres, going from 100 to 0.5 bar.

momentum flux convergence (colors in Figures 1(e)–(h)). Note that while the indirect cells in the extratropics (red colors in Figures 1(a)–(d)) are correlated with eddy momentum flux convergence (red colors in Figures 1(e)–(h)), and their associated eddy-driven jets (contours in Figures 1(a)–(d)), the direct cells in the extratropics (blue colors in Figures 1(a)–(d)) are correlated with eddy momentum flux divergence (blue colors in Figures 1(e)–(h)), and minimum zonal wind values. What causes these extratropical features to contract with atmospheric mass? To answer this, we first scale their meridional scale.

The contraction of the prominent flows in the atmosphere is also seen in spectral space, where the distribution of the barotropic (vertically averaged) kinetic energy is shifted to larger wavenumbers as the atmospheric mass increases (going from blue to red colors in Figure 12). The barotropic EKE is calculated following Boer & Shepherd (1983) as

$$\mathrm{bEKE}_n = \frac{1}{2}\sum_m \frac{n(n+1)}{a^2}\,|\Upsilon_m^n|^2, \tag{17}$$

where m and n are the zonal and total wavenumbers, respectively, and Υ is the horizontal barotropic streamfunction. Consistently, Kaspi & Showman (2015) showed that as the atmospheric mass increases the energy-containing wavenumber increases as well (see their Figure 15(b)). Because atmospheric jets hold most of the kinetic energy in the atmosphere, their meridional scale is found to follow the energy-containing wavelength (Figure 11(b)). The energy-containing wavelength is calculated as

$$L_e = 2\pi\left(\frac{a^2}{n_e(n_e+1)}\right)^{1/2}, \tag{18}$$

where n_e is the energy-containing wavenumber calculated as the inverse centroid of Equation (17),

$$n_e(n_e+1) = \frac{\sum_n \mathrm{bEKE}_n}{\sum_n \mathrm{bEKE}_n[n(n+1)]^{-1}}. \tag{19}$$

By incorporating the behavior of 2D turbulence in a two-layer quasi-geostrophic model, Rhines (1977) and Salmon (1978) described the energy flow in both the vertical and horizontal directions. As the energy cascades from the baroclinic mode (depth-dependent flow), which extracts potential energy from the mean flow, to the barotropic mode (depth-independent flow), it behaves as a two-dimensional fluid with an inverse energy and a forward enstrophy cascades. The inverse energy cascade is suppressed at the Rhines scale (Rhines 1975), due to the frequency mismatch of large-scale Rossby waves and small scale turbulent eddies. The inverse energy cascade, however, is not entirely suppressed, but keeps cascading in the zonal direction until reaching the zero zonal wavenumber, and zonal jets are formed. Thus, as substantial amount of MKE comes from barotropic eddies, the eddy-driven jets tend to have a more barotropic nature (depth-independent) than the subtropical jets (Figures 1(a)–(d)). This suggests that the Rhines scale should follow both the energy-containing and jet scales, as was shown to occur in 2D flow on a β-plane (e.g., Rhines 1975; Vallis & Maltrud 1993), two-layer models (e.g., Panetta 1993; Held & Larichev 1996; Lee 2005), idealized GCMs (e.g., O'Gorman & Schneider 2008; Jansen & Ferrari 2012; Chai & Vallis 2014; Chemke & Kaspi 2015, 2016a), and reanalysis data (e.g., Chemke et al. 2016a; Chemke & Kaspi 2016b).

The Rhines wavelength indeed follows the jets' width through all atmospheric mass simulations, with a clear isolated eddy-driven jet (Figure 11(c)). The Rhines wavelength is calculated as

$$L_\beta = 2\pi\left(\frac{(\mathrm{bEKE})^{1/2}}{\beta}\right)^{1/2},$$

where β is the meridional derivative of the Coriolis parameter. Because the β parameter does not vary between the different simulations, the change in the Rhines wavelength is due to the reduction of the barotropic EKE with atmospheric mass (Figure 12). As discussed in Section 4.1, this reduction is associated with the decrease in the meridional temperature gradient, which suppresses baroclinic instability processes that reduce the conversion of potential energy from the mean flow to kinetic energy.

5. Conclusions

In this study, we explore the effect of atmospheric mass on the general circulation. Atmospheric mass varies greatly between planets, and is clearly crucial for the atmospheric dynamics and habitability, and therefore understanding its affect on planetary climate is essential. Here, the dynamical-thermodynamical role of atmospheric mass on the planet's atmospheric circulation is studied using an idealized 3D ocean slab GCM, where the surface pressure is systematically varied (which is equivalent to changing the entire atmospheric mass) between 0.5 and 100 bar.

Two main thermodynamic processes vary with atmospheric mass (Figure 6). First, an increase in atmospheric mass reduces the convective fluxes (e.g., Goldblatt et al. 2009), leading to a cooler upper troposphere at mid-low latitudes. Second, the increase in the atmospheric heat capacity reduces the net radiative cooling (leading to warming) of the troposphere at high latitudes (Chemke et al. 2016b). These processes reduce the meridional temperature gradient and static stability, and

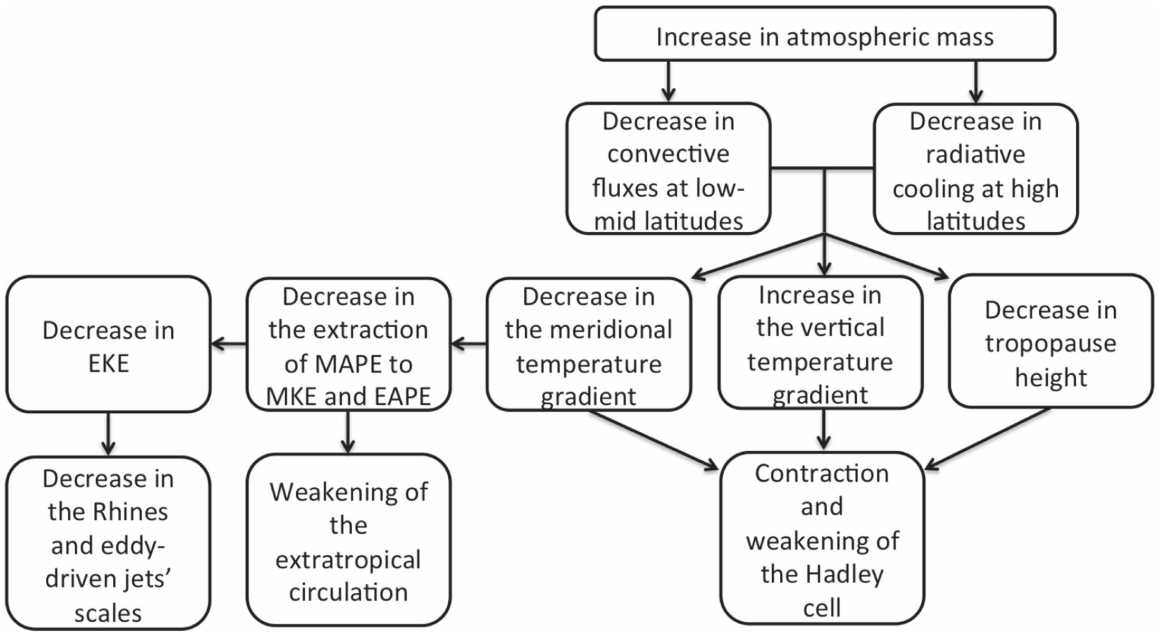

Figure 13. Flow chart summarizing the effects of atmospheric mass on both tropical and extratropical circulations.

lower the tropopause height (Figure 5). Note that as these processes are coupled (e.g., a reduction in radiative fluxes may result in a reduction in convective fluxes), the convective fluxes may only be responding to changes in the forcing and not directly to changes in atmospheric mass.

The resulting changes in the temperature field directly affect the circulation in both the tropics and extratropics (Figure 13). The Hadley circulation contracts as the atmospheric mass increases (Figure 2(a)). As its latitudinal extent is found to roughly follow the scaling of Held & Hou (1980) and Held (2000; Figure 2(b)), the reduction of the meridional temperature gradient, tropopause height, and static stability explain its contraction with atmospheric mass (Figure 4(a)). Similarly, the reduction in these parameters (Figure 9) also explains the weakening of the Hadley cell strength with atmospheric mass because it is also found to follow the scaling of Held & Hou (1980; Figure 8).

In the extratropics, the circulation also weakens with atmospheric mass (Figure 1). Studying the eddy-mean flow energy cycle shows that the reduction in the meridional temperature gradient reduces the extraction of mean available potential energy both to the eddies (e.g., by baroclinic instability processes through the reduction of the meridional eddy temperature fluxes) and to the mean kinetic energy (thermal wind balance; Figure 10). Because the extratropical circulation is driven by the differential warming of low and high latitudes, its reduction weakens the circulation.

An increase in atmospheric mass also contracts the extratropical circulation (Figure 1). The jets' width decreases with atmospheric mass and is found to follow both the energy-containing and Rhines wavelengths (Figure 11). Again, the reduction of the meridional temperature gradient, and its associated reduction in the contraction of available potential energy, reduces the EKE (Figure 12; e.g., Yuval & Kaspi 2016, 2017), which decreases the Rhines wavelength and hence the jets' width as well.

Because atmospheric mass is affected by its condensible species, it is interesting to compare the thermal and dynamical changes in our simulations with simulations where the mixing ratio of condensible species is increased (e.g., Pierrehumbert & Ding 2016). Although the physics is different, in both cases, the meridional temperature gradient decreases, which results in a more barotropic nature of the jets. The vertical temperature gradient behaves differently between these two cases, as it decreases with the mixing ratio of condensible gases and increases with atmospheric mass. While the former is related to a reduction of the moist adiabat, the later is related to the reduction of both the convective fluxes and net radiative cooling. Thus, in planets with heavy atmospheres that hold a high mixing ratio of condensible gases, the circulation might differ from our simulations.

The main goal of this study is to better understand the dynamical-thermodynamical role of atmospheric mass on the circulation. Thus, in order to keep the simulations as simple as possible, the simplified two-stream gray radiation scheme used in this study does not account for pressure broadening and Rayleigh scattering processes. Because these processes were also found to modulate the temperature field with atmospheric mass (Goldblatt et al. 2009; Wolf & Toon 2014), for a full understanding of the habitability of planets with different atmospheric mass, it is important to examine the flow properties in a full GCM, which accounts for all of the radiative ingredients that vary with atmospheric mass. Moreover, because the variety of exoplanets have a wide range of planetary parameters that differ from Earth's, it is also important to explore the effects of atmospheric mass under different planetary parameters (e.g., different obliquity and rotation rate, non-terrestrial planets, etc.) (e.g., Kaspi & Showman 2015; Kilic et al. 2017). Nonetheless, this study shows that high atmospheric mass planets may be more habitable due to both their higher surface temperature and weaker meridional temperature gradient, which allows higher temperature at high latitudes, and may help to maintain liquid

water on their surfaces. For example, the low meridional surface temperature gradient on Venus, in contrast to the high value on Mars, may be a result of the different atmospheric masses on these planets (e.g., Prinn & Fegley 1987; Read et al. 2015). Nevertheless, the lower rotation rate and obliquity of Venus likely also contribute to the lower meridional temperature gradient on Venus (Kaspi & Showman 2015).

We acknowledge support from the Israeli Space Agency, the Minerva foundation, the Lev Zion fellowship, and the Helen Kimmel Center for Planetary Science at the Weizmann Institute of Science.

References

Adams, E. R., Seager, S., & Elkins-Tanton, L. 2008, ApJ, 673, 1160
Betts, A. K. 1986, QJRMS, 112, 677
Betts, A. K., & Miller, M. J. 1986, QJRMS, 112, 693
Boer, G. J., & Shepherd, T. G. 1983, JAtS, 40, 164
Chai, J., & Vallis, G. K. 2014, JAtS, 71, 2300
Charnay, B., Forget, F., Wordsworth, R., et al. 2013, JGR, 118, 10414
Charney, J. G. 1947, J. of Meteorology, 4, 136
Charney, J. G., & Stern, M. E. 1962, JAtS, 19, 159
Chemke, R., Dror, T., & Kaspi, Y. 2016a, GeoRL, 43, 7725
Chemke, R., & Kaspi, Y. 2015, JAtS, 72, 3891
Chemke, R., & Kaspi, Y. 2016a, JAtS, 73, 2049
Chemke, R., & Kaspi, Y. 2016b, GeoRL, 43, 2723
Chemke, R., Kaspi, Y., & Halevy, I. 2016b, GeoRL, 43, 11414
Eady, E. T. 1949, Tell, 1, 33
Edmon, J. H. J., Hoskins, B. J., & McIntyre, M. E. 1980, JAtS, 37, 2600
Elkins-Tanton, L. T., & Seager, S. 2008, ApJ, 685, 1237
Forget, F., & Pierrehumbert, R. T. 1997, Sci, 278, 1273
Frierson, D. M. W., Held, I. M., & Zurita-Gotor, P. 2006, JAtS, 63, 2548
Goldblatt, C., Claire, M. W., Lenton, T. M., et al. 2009, NatGe, 2, 891
Goody, R. M., & Yung, Y. L. 1995, Atmospheric Radiation: Theoretical Basis (New York: Oxford Univ. Press)
Green, J. S. A. 1970, QJRMS, 96, 157
Hartmann, D. L. 1994, Global Physical Climatology (San Diego, CA: Academic)
Held, I. M. 1978, JAtS, 35, 572
Held, I. M. 1982, JAtS, 39, 412
Held, I. M. 2000, in Program in Geophysical Fluid Dynamics (Woods Hole, MA: Woods Hole Oceanographic Institute), Lectures
Held, I. M., & Hou, A. Y. 1980, JAtS, 37, 515
Held, I. M., & Larichev, V. D. 1996, JAtS, 53, 946
Holton, J. R. 1992, An Introduction to Dynamic Meteorology (3rd ed.; New York: Academic)
Jansen, M., & Ferrari, R. 2012, JAtS, 69, 695
Johnson, B., & Goldblatt, C. 2015, ESRv, 148, 150
Kaltenegger, L., Segura, A., & Mohanty, S. 2011, ApJ, 733, 35
Kaspi, Y., & Showman, A. P. 2015, ApJ, 804, 60
Kasting, J. F., & Catling, D. 2003, ARA&A, 41, 429
Kavanagh, L., & Goldblatt, C. 2015, E&PSL, 413, 51
Kilic, C., Raible, C. C., Stocker, T. F., & Kirk, E. 2017, P&SS, 135, 1
Lee, S. 2005, JAtS, 62, 2482
Lorenz, E. N. 1955, Tell, 7, 157
Lorenz, R. D., McKay, C. P., & Lunine, J. I. 1999, P&SS, 47, 1503
Marty, B., Zimmermann, L., Pujol, M., Burgess, R., & Philippot, P. 2013, Sci, 342, 101
Nishizawa, M., Sano, Y., Ueno, Y., & Maruyama, S. 2007, E&PSL, 254, 332
O'Gorman, P. A., & Schneider, T. 2008, JAtS, 65, 524
Panetta, R. L. 1993, JAtS, 50, 2073
Pedlosky, J. 1987, Geophysical Fluid Dynamics (New York: Springer)
Peixoto, J. P., & Oort, A. H. 1992, Physics of Climate (New York: AIP)
Phillips, N. A. 1954, Tell, 6, 273
Pierrehumbert, R. T., Abbot, D. S., Voigt, A., & Koll, D. 2010, AREPS, 39, 417
Pierrehumbert, R. T., & Ding, F. 2016, RSPSA, 472, 20160107
Prinn, R. G., & Fegley, B. 1987, AREPS, 15, 171
Read, P. L., Lewis, S. R., & Mulholland, D. P. 2015, RPPh, 78, 125901
Rhines, P. B. 1975, JFM, 69, 417
Rhines, P. B. 1977, in The Sea, Vol. 6, ed. E. D. Goldberg (New York: Wiley), 189
Salmon, R. 1978, GApFD, 10, 25
Schneider, T. 2006, AREPS, 34, 655
Schneider, T., & Walker, C. C. 2006, JAtS, 63, 1569
Seager, S. 2013, Sci, 340, 577
Selsis, F., Kasting, J. F., Levrard, B., et al. 2007, A&A, 476, 1373
Simmons, A. J., & Hoskins, B. J. 1978, JAtS, 35, 414
Som, S. M., Buick, R., Hagadorn, J. W., et al. 2016, NatGe, 9, 448
Som, S. M., Catling, D. C., Harnmeijer, J. P., Povlika, P. M., & Buick, R. 2012, Natur, 484, 359
Vallis, G. K. 2006, Atmospheric and Oceanic Fluid Dynamics (Cambridge: Cambridge Univ. Press)
Vallis, G. K., & Maltrud, M. E. 1993, JPO, 23, 1346
von Paris, P., Gebauer, S., Godolt, M., et al. 2010, A&A, 522, A23
Wolf, E. T., & Toon, O. B. 2014, AsBio, 14, 241
Wordsworth, R. D., Forget, F., Selsis, F., et al. 2010, A&A, 522, A22
Wordsworth, R. D., Forget, F., Selsis, F., et al. 2011, ApJL, 733, L48
Yuval, J., & Kaspi, Y. 2016, JAtS, 73, 1709
Yuval, J., & Kaspi, Y. 2017, JAtS, 74, 1651